A Thermal-Flywheel Approach to Distributed Temperature Control in Microchannel Reactors

Richard C. Pattison and Michael Baldea
Dept. of Chemical Engineering, The University of Texas at Austin, Austin, TX 78712

DOI 10.1002/aic.13991
Published online January 24, 2013 in Wiley Online Library (wileyonlinelibrary.com)

Microchannel reactors are a promising route for monetizing distributed natural gas resources. However, intensification and miniaturization represent a significant challenge for reactor control. Focusing on autothermal methane-steam reforming reactors, a novel microchannel reactor temperature control strategy based on confining a layer of phase-change material (PCM) between the reactor plates is introduced. Melting-solidification cycles, which occur with latent heat exchange at constant temperature, allow the PCM layer to act as an energy storage buffer—a "thermal flywheel"—constituting a distributed controller that mitigates temperature excursions caused by fluctuations in feedstock quality. A novel stochastic optimization algorithm for selecting the PCM layer thickness (i.e., distributed controller "tuning") is introduced. Furthermore, a hierarchical control structure, whereby the PCM layer is complemented by a supervisory controller that addresses persistent disturbances, is proposed. The proposed concepts are illustrated in a comprehensive case study using a detailed two-dimensional reactor model. © 2013 American Institute of Chemical Engineers *AIChE J*, 59: 2051–2061, 2013
Keywords: reactor analysis, optimization, mathematical modeling, process control

Introduction

Natural gas deposits located in remote areas (referred to as "stranded gas") constitute a significant energy resource at the global level, with reserves recently estimated at 170 trillion cubic meters (6000 trillion cubic feet).[1] Natural gas is also present in considerable quantities as associated gas in oil reservoirs, coal mines, and landfills. Despite the vast energy resources that they contain, most stranded gas reservoirs are presently undeveloped, whereas about two-thirds of the associated natural gas that is inevitably obtained in the oil production process are reinjected, and the remainder is flared. Available data[2] indicate that in 2011 about 140 billion cubic meters of natural gas were flared (with 7 billion in the United States alone), wasting 4500 billion megajoules of energy and releasing 265 million tons of CO_2 in the atmosphere. Further environmental impacts (such as the release of volatile organic compounds (VOC), sulfuric oxides (SOX), and nitric oxides (NOX), and formation of ozone) can evidently be inferred.

An often-invoked reason for this vast energy resource to remain unexplored is economical. Indeed, the traditional approach for transporting natural gas and delivering it to end users entails the construction of a pipeline, a costly undertaking that is not justified when the resource is not available in large quantities or is located in a remote, unaccessible area. Further consideration of the underlying reasons of failing to monetize stranded and associated gas deposits points, however, in a different direction. Such resources could, in principle, be exploited economically by converting them to other products, with either higher economical value, cheaper transportation logistics, or both, including liquefied natural gas, hydrogen, or Fischer–Tropsch liquids (synthetic crude). Evidently, the condition is that such conversion processes be carried out at the source/wellhead. However, existing liquefaction and chemical processing technologies, including steam-methane reforming (SMR) and Fischer–Tropsch synthesis, have proven viable only when used on a large scale[3–6]; their economic performance is severely degraded when processing small quantities of gas. In light of the above, stranded and associated gas deposits remain unaccessible due, in fact, to a vexing and paradoxical technology gap, whereby a family of processes using natural gas as a feedstock have very good scale-up performance, yet scale down very poorly.

As a result, recent developments advocate process intensification as a pathway to the development of small-scale plants that facilitate localized production.[7] The thesis of process intensification is "to do more with less," minimizing transfer and transport limitations such that the process is governed by chemical reaction rates.[8] Catalytic plate microchannel reactors (CPRs) have proven to be one of the most successful and promising solutions in this area. CPRs consist of alternating millimeter-sized channels, separated by catalytically coated plates.

In the present article, we focus on autothermal microchannel reactors for SMR, an important means for decentralized hydrogen production and a potential intermediate step in small-scale Fischer–Tropsch synthesis. In microchannel SMR CPRs, the endothermic reforming reactions are supported by the exothermic catalytic combustion of methane, occurring

Correspondence concerning this article should be addressed to M. Baldea at mbaldea@che.utexas.edu.

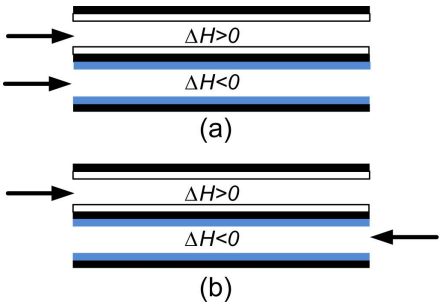

Figure 1. Flow configurations for microchannel reactors coupling exothermic and endothermic reactions.

[Color figure can be viewed in the online issue, which is available at wileyonlinelibrary.com.]

in parallel, alternate channels. Both cocurrent (Figure 1a) and counter-current (Figure 1b) designs have been explored,[9–13] confirming that CPRs can achieve high conversions with an order-of-magnitude size reduction compared with conventional units. However, these studies have also indicated several potential operational issues, such as flow maldistribution and local temperature rises (hotspots) with deleterious effects on the integrity of the catalyst coatings and supporting plates. Several design modifications have been proposed to mitigate these issues, including using catalysts with nonuniform activity,[14] distributed fuel feeds,[15] reverse flow configurations,[15,16] or offsetting the catalyst coating in the reforming and combustion channels.[13,17]

Furthermore, CPR operation is subject to fluctuations in reforming flow and/or gas composition, with potentially serious consequences. For example, a rapid drop in reforming flow rate can cause significant temperature increases in the reactor and must be compensated, for example, by reducing the fuel flow rate. Implementing an appropriate control system is, therefore, an imperative requirement in practical situations. Addressing this need is, however, hindered by the inherent difficulties of controlling distributed-parameter systems. Practical considerations pertaining to the design and dimensions of CPRs also limit the availability of distributed measurements (e.g., the constructive challenges and cost of locating temperature sensors in a multiplate stack are prohibitive) and actuators (likewise, it is not economically feasible to control the flow to each channel).

In this article, we concentrate on autothermal reactors producing hydrogen via methane-steam reforming and introduce a novel hierarchical control structure for CPRs. Distributed temperature control is based on the unconventional use of a layer of phase-change material (PCM) confined between the reactor plates. Through its melting-solidification cycles, which occur with latent heat exchange at constant temperature, the PCM layer acts as an energy storage buffer (i.e., a "thermal flywheel"), which mitigates temperature excursions occurring due to inherent fluctuations in feedstock flow rate and quality. The supervisory layer consists of a model-based feedback–feedforward nonlinear controller. In keeping with the unconventional nature of the proposed distributed control system, we also introduce a novel stochastic optimization method for selecting the PCM layer thickness (i.e., for distributed controller "tuning"). Throughout the article, we use a comprehensive simulation case study involving a detailed two-dimensional (2-D) reactor model to illustrate the proposed concepts and to showcase the excellent performance and robustness of our novel control approach.

System Description

Nominal reactor model

We consider as the nominal system a CPR consisting of a catalytic plate with the adjacent reforming and combustion channels, in a counter-current flow configuration (Figure 2). We model the gas phase in each channel as a 2-D laminar convection-diffusion-reacting flow, consider 2-D heat conduction in the wall plate, and use a one-dimensional reaction-diffusion equation to capture the reactant composition in the catalyst layers. The boundary conditions are set up as no-flux (the channel outlets), equal flux (at the fluid–solid interface), and symmetry (at the channel centers). The inlet velocity profile is assumed to be fully developed parabolic laminar flow between two infinite parallel plates. The detailed model equations can be found in Appendix A. An offset catalyst distribution[13] is used to provide an optimal synchronization of the heat generation and consumption fluxes in the exothermic and, respectively, endothermic channels.

We assume that the following set of reactions is occurring in the reforming channel, with the reaction kinetics derived by Xu and Froment.[18]

- Methane steam reforming (1)

$$CH_4 + H_2O \rightleftharpoons CO + 3H_2$$

$$\Delta H = +206\ \mathrm{kJ/mol}$$

- Water–gas-shift (2)

$$CO + H_2O \rightleftharpoons CO_2 + H_2$$

$$\Delta H = -41\ \mathrm{kJ/mol}$$

- Reverse methanation (3)

$$CH_4 + 2H_2O \rightleftharpoons CO_2 + 4H_2$$

$$\Delta H = +165\ \mathrm{kJ/mol}$$

The catalytic combustion of methane occurs in the combustion channels:

- Methane combustion (4)

$$CH_4 + 2O_2 \rightarrow CO_2 + 2H_2O$$

$$\Delta H = -803\ \mathrm{kJ/mol}$$

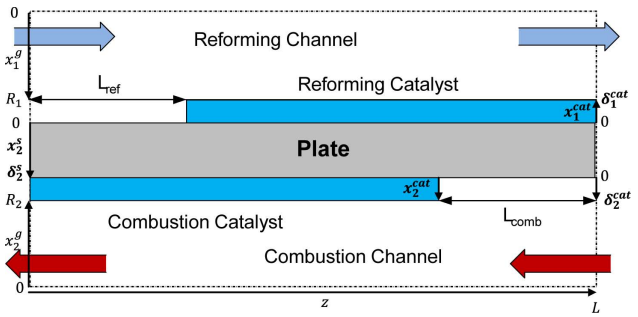

Figure 2. Nominal case catalytic plate reactor model configuration.

[Color figure can be viewed in the online issue, which is available at wileyonlinelibrary.com.]

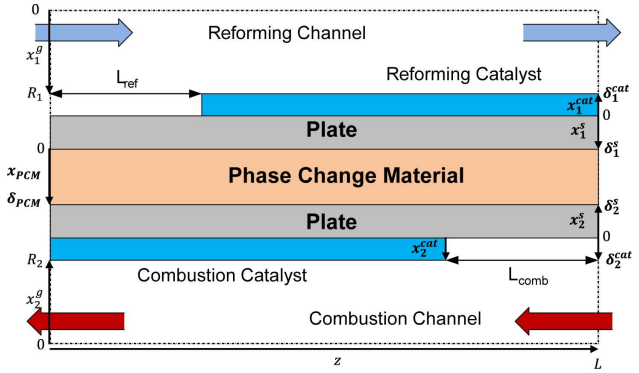

Figure 3. Catalytic plate reactor model with a PCM confined within the solid wall.

[Color figure can be viewed in the online issue, which is available at wileyonlinelibrary.com.]

The catalytic combustion rate is assumed to be first order with respect to methane and zero order with respect to oxygen. Homogeneous combustion has a measurable impact at high temperatures and is accounted for, with the reaction being of order −0.3 and 1.3 in methane and oxygen, respectively. Complete data concerning the chemical reactions are available in our previous study.[13]

Reactor with PCM layer

The melting and solidification of materials are phase transformations that involve latent heat exchange with the environment, occurring at constant temperature. Owing to this property, PCMs have found applications in thermal energy storage,[19] and temperature regulation for microelectronics[20,21] and building walls.[22] Through its melting-solidification cycles, the PCM acts as an energy storage buffer that mitigates temperature excursions. Thus, confining a PCM with an appropriately selected melting point (i.e., with a phase-transition temperature above the maximum nominal operating temperature and below the maximum safe operating temperature) between the plates of a CPR, as illustrated in Figure 3, has the potential to prevent local temperature rises in the presence of disturbances which would, under other circumstances, give rise to hotspots.

To investigate the potential for using PCMs for local temperature control, we extended the model in the previous section considering that the channels are separated by two plates confining a PCM layer. To facilitate the simulation of melting and solidification phenomena, the PCM layer is modeled using the enthalpy, rather than temperature, as the state variable (i.e., the celebrated Stefan formulation)

$$\rho^{\mathrm{p}}\frac{\partial H^{\mathrm{p}}}{\partial t}=\frac{\partial}{\partial z}\left(k^{\mathrm{p}}\frac{\partial T^{\mathrm{p}}}{\partial z}\right)+\frac{\partial}{\partial x^{\mathrm{p}}}\left(k^{\mathrm{p}}\frac{\partial T^{\mathrm{p}}}{\partial x^{\mathrm{p}}}\right) \tag{1}$$

where ρ is the density, H^p is the enthalpy, and k is the thermal conductivity of the PCM. The PCM temperature, T is calculated from enthalpy as

$$T^{\mathrm{p}}=\begin{cases} T_{\mathrm{r}}+\dfrac{H^{\mathrm{p}}}{\rho^{\mathrm{p}}c_{\mathrm{s}}} & H^{\mathrm{p}}<c_{\mathrm{s}}(T_{\mathrm{m}}-T_{\mathrm{r}}) \\ T_{\mathrm{m}} & c_{\mathrm{s}}(T_{\mathrm{m}}-T_{\mathrm{r}})\le H^{\mathrm{p}}<c_{\mathrm{s}}(T_{\mathrm{m}}-T_{\mathrm{r}})+\lambda \\ T_{\mathrm{m}}+\dfrac{H^{\mathrm{p}}-\lambda-c_{\mathrm{s}}(T_{\mathrm{m}}-T_{\mathrm{r}})}{c_{\mathrm{l}}} & H^{\mathrm{p}}\ge c_{\mathrm{s}}(T_{\mathrm{m}}-T_{\mathrm{r}})+\lambda \end{cases} \tag{2}$$

where T_r is a reference temperature, c_s and c_l are the specific heats of the solid and liquid PCM, respectively, T_m is the PCM melting temperature, and λ is the latent heat of fusion of the PCM.

A "mushy region" approximation[23] was used to alleviate the numerical difficulties associated with the discontinuity of the values of thermal conductivity, heat capacity, and density at the melting front. This approximation consists of defining a melting region in which the transition between phases occurs gradually, rather than discontinuously as is the case at the melting front. This assumption is captured by defining an additional (fictitious) variable, the melt fraction f, whose values vary between $f = 1$ (in the solid phase) and $f = 0$ (in the melt)

$$f=\begin{cases} 1 & T^{\mathrm{p}}<T_{\mathrm{m}} \\ \dfrac{H^{\mathrm{p}}-c_{\mathrm{s}}(T_{\mathrm{m}}-T_{\mathrm{r}})}{\lambda} & T^{\mathrm{p}}=T_{\mathrm{m}} \\ 0 & T^{\mathrm{p}}>T_{\mathrm{m}} \end{cases} \tag{3}$$

Then, the values of the aforementioned physical properties in the melting region are computed as continuous, smooth linear combinations of their values in the solid and, respectively, liquid phases. For example, the heat capacity in the melt region can be expressed as $C_{\mathrm{p,mr}}=fC_{\mathrm{p,s}}+(1-f)C_{\mathrm{p,l}}$

Remark 1. The choice of PCM is influenced by the desired operating temperatures which, in turn, strongly influence the potential onset of carbon deposition and catalyst deactivation/sintering. It is very important to note that, in addition to a suitable melting point, the material chosen for the PCM layer should not impede on the heat transfer between the exothermic and endothermic channels. Consequently, materials with high thermal conductivity are preferred. Although the experimental validation of the proposed designs is beyond the scope of this work, an initial screening suggests constructing the reactor of RA446 high-chromium steel with copper (melting point 1084°C) as the PCM, or of 316 L stainless steel with a cobalt–titanium eutectic (melting point 1020°C) as the PCM. Using a brass PCM layer will further lower operating temperatures; depending on composition, the melting temperature of brass ranges from 900 to 1000°C, with other physical properties being similar to copper.

Another potential challenge is associated with the discontinuous change in density at the PCM melting front. Expansion upon PCM melting can lead to local modifications in the geometry of the walls. However, for most metals, this expansion is quite small (e.g., the liquid density of copper is 95% of the solid density at the melting point) and, consequently, we expect that such geometric effects will not be deleterious. Furthermore, the malleability of most wall materials is high at elevated temperatures, which should increase tolerance to such events.

Simulation Study: Steady-State System Performance

We consider a practical CPR system, whose parameters are presented in Table 1 using copper as the PCM. The physical properties of copper within the operating temperatures are shown in Table 3. Note that material compatibility aspects (e.g., the potential diffusion of the melted PCM in the solid plates) were not investigated in this study.

The mathematical models of the nominal system and of the PCM-enhanced reactor were implemented and solved in gPROMS.[25] Backward finite differences were used to discretize the axial domain in the reforming channel, the reforming catalyst layer, and the solid wall on the reforming side.

Table 1. Reactor System Details

Parameter	Value
Reactor length	0.6 m
Reforming channel half-height	1.0 mm
Combustion channel half-height	1.0 mm
Reforming catalyst height	20 μm
Combustion catalyst height	20 μm
L_{ref}	9.0 cm
L_{comb}	15 cm
Reforming inlet temperature	793.15 K
Combustion inlet temperature	793.15 K
Reforming inlet composition	19.11% CH_4
	72.18% H_2O
	2.94% CO_2
	0.29% H_2
	5.48% N_2
Combustion inlet composition	5.26% CH_4
	22.09% O_2
	72.65% N_2

Forward finite differences were used to discretize the axial domain in the combustion channel, the combustion catalyst layer, and the solid wall on the combustion side. A central finite difference discretization was used for the axial (z) domain of the PCM, and orthogonal collocation of finite elements was used for discretizing the partial derivative terms in the longitudinal (r) direction in every layer. For the axial domain, a 30-node mesh was used, and in the longitudinal domains, three nodes were used in every layer other than the PCM, which had four nodes. No significant changes in the numerical results were noticed upon using a finer discretization.

Figures 4–6 compare the axial temperature distribution, conversion, and heat flux for the base-case reactor and the PCM-enhanced reactor at the nominal operating conditions. Conversion is calculated by integrating the local mass flow rate through each channel

$$X_j(z) = 1 - \frac{\int_0^{R_j} \rho_j^g u_{z_j} \omega_{CH_{4_j}}^g dx_j^g|_z}{\int_0^{R_j} \rho_j^g u_{z_j} \omega_{CH_{4_j}}^g dx_j^g|_{z=0(j=1),z=L(j=2)}} \quad (4)$$

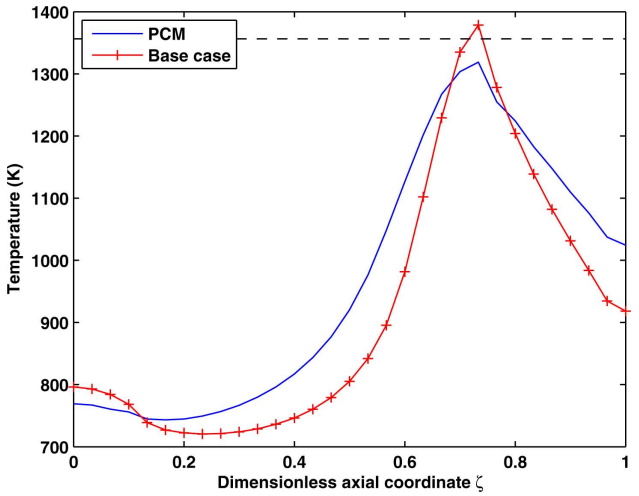

Figure 4. Axial temperature at steady state for the PCM-enhanced CPR compared to the base-case CPR.

[Color figure can be viewed in the online issue, which is available at wileyonlinelibrary.com.]

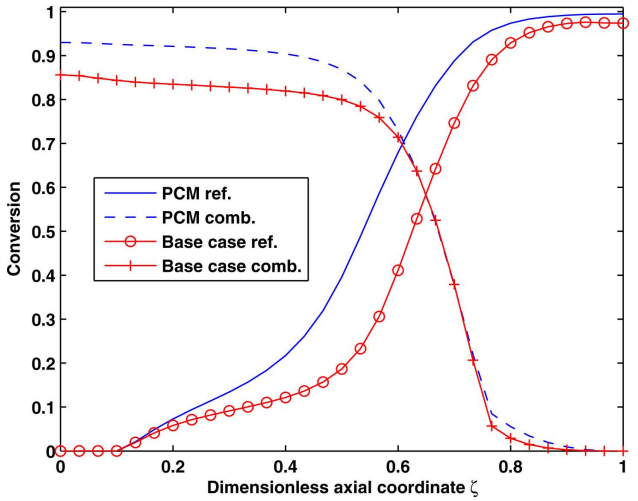

Figure 5. Steady-state axial conversion profiles for the PCM-enhanced CPR compared to the base-case CPR.

Combustion flow occurs from right to left and reforming from left to right. [Color figure can be viewed in the online issue, which is available at wileyonlinelibrary.com.]

Notice that confining a thermally conductive PCM layer between the reactor plates of a CPR does not degrade the steady-state reactor performance. Rather, it improves performance with increased conversion in the combustion channel, a more evenly distributed heat flux, a more uniform temperature distribution along the axial coordinate (owing to the high thermal conductivity of the copper layer), and a reduction of the maximum reactor temperature, which prolongs the life of the catalyst and ensures the structural integrity of the reactor.

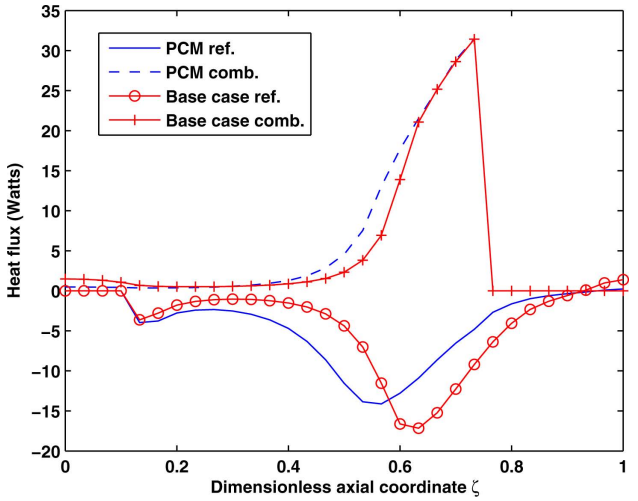

Figure 6. Steady-state axial heat fluxes for the PCM-enhanced CPR compared to the base-case CPR.

[Color figure can be viewed in the online issue, which is available at wileyonlinelibrary.com.]

Table 2. PCM Parameters[24]

Parameter	Value	Units
PCM	Copper	–
Melting temperature	1356	K
Latent heat of melting	231,000	kJ/kg
Solid density	$-0.375T^{p}+9130$	kg/m3
Liquid density	$-0.460T^{p}+8800$	kg/m3
Solid heat capacity	481	J/(kg K)
Liquid heat capacity	531	J/(kg K)
Solid thermal conductivity	$-0.0899T^{p}+438$	W/(m K)
Liquid thermal conductivity	$0.0497T^{p}+89.7$	W/(m K)

Latent Energy Storage-Based Temperature Control

Hierarchical control structure

Under typical operating conditions, CPRs are subject to inherent fluctuations in the flow rate, composition, and feed temperature of the reactants in both channels. Fluctuations that cause a reduction of the rate at which energy is consumed by the endothermic reactions (e.g., a reduction of the flow rate in the reforming channel) are likely to have the most deleterious effects. Their result is an excess of energy generated by combustion, with the evident potential for large, local temperature increases. In such cases, the confined PCM acts as a "buffer," absorbing the excess heat at constant temperature and preventing the formation of hotspots. Evidently, this temperature control effect is limited by the thickness of the PCM layer. It disappears once the material is completely melted, at which time (assuming persistent disturbances) the reactor temperature will continue to rise.

As a consequence, the implementation of PCM-based temperature control must be carried out as part of a hierarchical control structure, whereby the PCM layer acts as a fast, distributed controller, and a supervisory controller acts over a longer time horizon to mitigate persistent disturbances.

Practical considerations limit the supervisory controller to a boundary-control configuration, with the fuel flow rate to the combustion channels being the only available manipulated variable. Similar practical considerations also limit the efficiency of this controller as a stand-alone control system (i.e., without the PCM layer used for distributed control). Specifically, the effectiveness of the boundary controller is strongly dependent on (and limited by) flow distribution among the numerous (possibly hundreds) millimeter-sized channels that form a reactor stack. As mentioned before, it is not possible to control the flow to individual channels; rather, one has to rely on a distribution device (header) to direct the stack inlet to each channel. Uniform and equal flow rates to each channel cannot be established instantaneously and maldistribution can occur. Consequently, if the supervisory controller is used without the PCM layer, the time delays associated with flow distribution could be sufficiently long for hotspots to form in channels with preferentially high fuel flow, which endanger the catalysts and structural integrity of the reactor.

Optimal calibration of PCM geometry for distributed control performance

Physical arguments indicate that if the thickness of the PCM layer is much smaller than the thickness of the catalytic plates (i.e., $\delta_{PCM} \ll \delta_s^1$ and $\delta_{PCM} \ll \delta_s^2$), the complete (local) melting of the material will occur rapidly in the presence of disturbances, and the temperature control effect of the PCM will be short lived. In this case, however, the PCM layers will not contribute significantly to the total height and mass of the reactor stack. Conversely, if a thicker PCM layer is used, local temperature control will extend over a longer period of time, with the disadvantage that the reactor stack will be larger. In practical applications, stack height and mass are important factors: the operating principle of CPRs is centered on flexibility and deployability in a broad range of environments, including mobile applications such as offshore platforms. The cost of the PCM-enhanced reactor is largely determined by manufacturing costs, rather than the cost of the PCM itself, and will likely not vary significantly as a function of the cost of the PCM. For example, considering a reactor with a height of 1 m, a width of 0.5 m, and a length of 0.6 m, the cost of the copper is around $2000 assuming bulk pricing.[26] However, the public availability of CPR price information is very limited, and it is, therefore, difficult to determine the exact contribution of this amount to the total reactor cost.

In light of the above, the dynamic effect of the PCM layer is directly dependent on its geometry, and determining the layer thickness is akin to tuning a controller. Evidently, the PCM layer thickness is fixed at manufacturing and such tuning cannot be carried out online. Dynamic optimization represents a natural framework for determining, off-line, the optimal thickness of the PCM layer. Intuitively, the objective function should account for (1) the deviation of the peak reactor temperature from a desired target and (2) the weight penalty of increasing the thickness of the PCM layer. A further complication arises from the fact that the operation of the reactor is subject to fluctuations in the reforming flow rate. Therefore, the optimization calculations should be stochastic and aimed at minimizing the likelihood of the peak temperature exceeding the temperature target, rather than considering the worst-case scenario of a significant disturbance (which, as mentioned before, would result in a very large PCM layer thickness).

In this section, we introduce a novel method for performing such optimization calculations. The proposed method is based on uniting dynamic optimization with concepts from nonlinear system identification. Specifically, the reforming flow rate is represented as a pseudorandom multilevel sequence[27,28] (PRMS), which is imposed on the reactor during the dynamic optimization iterations.

The objective function to be minimized (Eq. 5) consists of the time integral of the deviations of the temperature from the PCM melting point, and a penalty for the thickness of the PCM

$$J = c \times \delta^{p} + \int_0^{t_{final}} H(T_{max}(t) - T_m) \times (T_{max}(t) - T_m) dt \qquad (5)$$

Table 3. Optimization Algorithm

Initial guess for PCM thickness, δ^0
while $\| \delta_k^p - \delta^{p^*} \| \geq \epsilon$ **do**
Simulate reactor from $t=0$ to t_{final} imposing the PRMS disturbance
Calculate objective function (Eq. 5)
Calculate objective function gradients
Update δ^p
end while

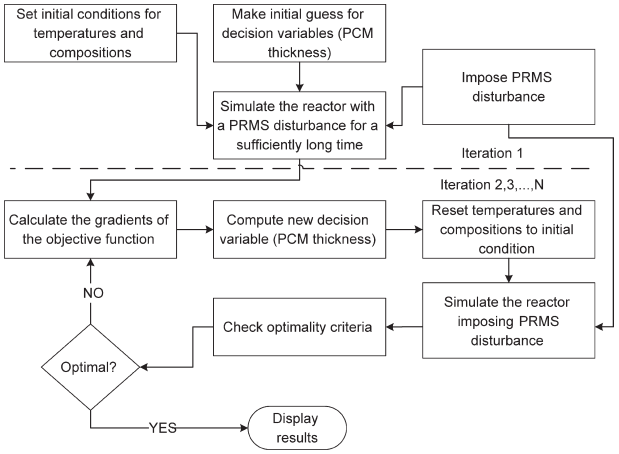

Figure 7. Diagram of the optimization algorithm.

where δ^{p} is the PCM thickness, c is the cost penalty per unit thickness, T_{max} is the maximum temperature in the z direction, and $H(x)$ is the Heaviside function. The optimization time horizon, t_{final}, is fixed.

The optimization calculations proceed according to the algorithm in Table 2, which is illustrated in more detail in Figure 7.

Remark 2. Imposing the PRMS disturbance in the course of the dynamic simulation, along with the time-integral objective function and a sufficiently long time horizon, allows the system to efficiently sample its possible states in a Monte Carlo fashion. In the present case, we minimize a time-integral objective function and do not account for path/trajectory constraints. However such constraints can be easily imposed.

Supervisory control

As mentioned earlier, the role of the supervisory controller is to reject persistent disturbances in the flow rate and composition of the feed streams. Fulfilling this role is limited by practical considerations to a boundary-control approach, where a limited subset of the inputs and outputs of the CPR can be measured or manipulated. The former includes the output temperatures of the two channel sets, whereas the latter is likely confined to altering the flow rate of the fuel stream. Composition measurements can, in principle, be obtained via gas chromatography, but the cost of the associated hardware is high.

As a consequence, the structure of the supervisory controller should follow a combined feedback–feedforward paradigm, with the feedback component relying on temperature measurements from the reforming channel, and the feedforward component using information provided by a flow sensor placed on the reforming channel feed stream. A controller design approach is, on the other hand, more difficult to prescribe *a priori*. In principle, any of the available inversion- or optimization-based linear or nonlinear controller design methods are applicable. However, the choice of controller design is complicated by the distributed-parameter nature of the system and will depend on the availability of an appropriate mathematical model. Although the closed-loop time constant for the supervisory control tier can be chosen to be relatively long, it is evident that the large dimensions and stiff, multiscale nature of the detailed mathematical model described in the previous sections prohibit its use for online applications, in particular when optimization calculations are necessary, for example, in the case of model-predictive control.

Simulation Study (Continued): Controller Design and Performance

PCM layer optimization

We used the algorithm described earlier to determine the optimal thickness of the PCM distributed control layer for a reactor with the nominal parameters presented in Table 1. We assumed that the reforming flow rate (as determined by the inlet velocity to the reforming channels) can exhibit both positive and negative variations, with an amplitude of up to 50% of the nominal value, which occur with equal probability.

To compute the PRMS required by the proposed optimization algorithm, a frequency analysis on the nominal system was performed. Based on physical considerations, the PCM layer must reject disturbances with frequencies within a bounded range. Due to the elevated thermal inertia of the plates and PCM layer compared with the gas phase, the reactor will naturally filter high-frequency disturbances. Conversely, the time constant for flow distribution to the channels and the supervisory closed-loop time constant dictate the lower limit of the frequency range; lower-frequency disturbances are addressed by the supervisory controller. The upper bound of the frequency range was computed using a simple linear analysis, whereby a series of disturbance step tests were performed on the base-case reactor to obtain an approximate first-order transfer function model relating the maximum plate temperature to the reforming flow rate. Equation 6 shows the first-order transfer function model that best approximates the base-case system.

$$\tilde{T}_{max} = \frac{-0.20}{1+6.66s}\tilde{u}^{0}_{max} \tag{6}$$

where $\tilde{T}_{max}$ represents the deviation from the nominal maximum temperature, and $\tilde{u}^{0}_{max}$ represents the deviation of the reforming flow.

In our controller design, we assumed that disturbances with frequencies slightly above the corner frequency (10^{-1} rad/s) are filtered by the plates, and frequencies one order of magnitude smaller will be rejected by the yet-to-be designed supervisory controller. These results indicate a duration of the PRMS steps, $t_{PRMS} \in [50\,s, 350\,s]$. This also suggests that the closed-loop time constant for the supervisory controller should be selected to be close to the upper bound of this interval.

Figure 8 shows the 30-level PRMS used in the optimization and the response of the reactor to these excitations, in the absence of the supervisory control layer.

We used the algorithm described earlier to minimize the design objective function (5), subject to satisfying all the equations in the reactor model. Notice that the solution of this problem depends on the choice of the cost penalty c in Eq. 5, which is influenced by the type of service and location that the reactor will be placed in. Low cost penalties will result in a thicker PCM layer and larger reactor stacks, with the PCM providing a strong temperature control effect.

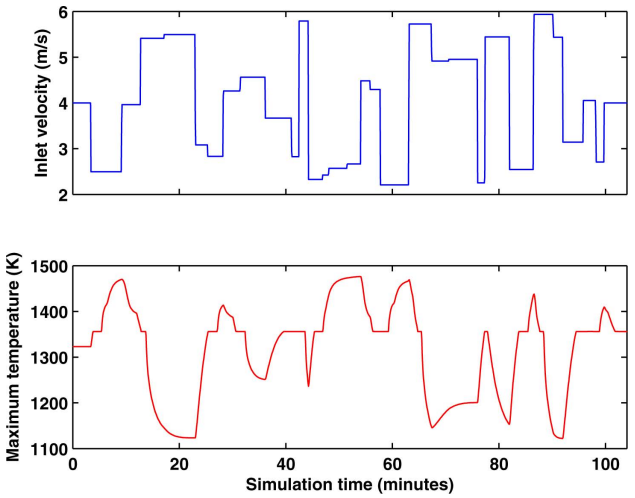

Figure 8. Top: Multilevel random sequence of reforming inlet velocity. Bottom: corresponding response of the PCM-enhanced system (maximum reactor temperature).

The objective function is calculated by integrating the maximum temperature throughout the simulation when it is above the melting point. [Color figure can be viewed in the online issue, which is available at wileyonlinelibrary.com.]

Conversely, increasing c will diminish reactor stack size as well as the temperature regulation efficiency of the PCM layer. To investigate its effect on the solution of the optimization problem, we solved the optimization problem for several choices of c, with the results displayed in Figure 9. As expected, lower-cost penalties result in a reactor with a thicker PCM layer.

Supervisory control

To compensate for sustained disturbances in the inlet flow rate to the reforming channel, we derived an input–output linearizing feedback–feedforward controller,[29] which adjusts the inlet flow to the combustion channel based on measurements of the reforming flow and the exit reforming temperature, requesting a first-order closed-loop of the form

$$T^{\text{ref}}\big|_{z=L} + \tau_{\text{CL}} \frac{dT^{\text{ref}}\big|_{z=L}}{dt} = T^{\text{sp}} \tag{7}$$

where τ_{CL} is the closed-loop time constant (selected to be 240 s). A complete description of the derivation of the supervisory controller is presented in Appendix B.

Control performance

We first performed simulation studies to compare the transient operation of the PCM-enhanced CPR without the supervisory controller with the base-case reactor. The results shown below consider the worst-case scenario of a thin PCM layer, corresponding to the maximum value of the penalty c as described earlier. In this case, the optimal PCM layer thickness is $\delta = 0.56$ mm, and the additional confined material accounts for about 18% of the total reactor volume and 51% of the total reactor weight. Table 4 displays parameters used in the case study highlighting the differences between the two systems.

Figure 10 presents the evolution of the peak reactor temperature (notice that the location of the temperature peak in the z direction may shift in time), in response to a 50% decrease in the inlet velocity of reforming flow. As the reforming flow rate drops, the temperature in the reactor is expected to rise due to a decrease in the endothermic reaction rate. As seen in Figure 10, the rise time to a new steady state is much longer for the PCM-enhanced reactor than in the base case. There is an initial temperature rise to the melting point, then the temperature remains constant at the melting point until the layer has completely melted. Subsequently, the temperature rises slowly to the new steady-state maximum temperature as melting continues in the axial direction. Conversely, the temperature in the base-case CPR rises very quickly, reaching a high value at which the structural integrity of the reactor would be compromised.

Subsequently, we performed simulations with the supervisory controller operating in closed loop. In Figures 11a,b, a 300 min closed-loop operating period is simulated, with sustained 40% drops, first in the reforming flow rate subsequently in the reforming inlet composition, followed by 30% simultaneous change in both aforementioned disturbances. The changes in flow rate are simulated as variations in inlet velocity, whereas the composition change is assumed to result in (and be reflected by) a decrease in the heat of reaction of the steam-reforming reactions. The results evince excellent control performance. It is also remarkable that, although the controlled variable is the reforming channel output temperature, the proposed control system is successful at preventing the advent of hotspots: the maximum longitudinal reactor temperature (Figure 11a) only exceeds the melting temperature of the PCM on a brief occasion, which corresponds to a dramatic 40% drop in the amount of heat absorbed by the reforming reactions.

Conclusions

In this article, we proposed a novel temperature control concept for plate reactors with microscopic channels. Our approach consists of confining a layer of PCM between the

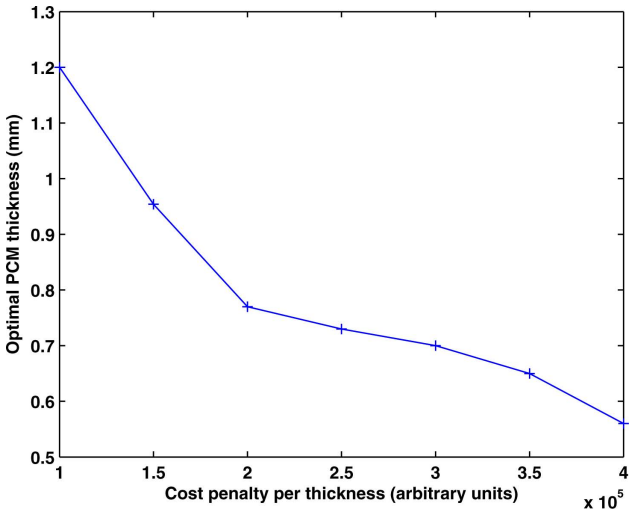

Figure 9. Optimal PCM thickness as a function of the cost penalty *c*.

[Color figure can be viewed in the online issue, which is available at wileyonlinelibrary.com.]

Table 4. Case Study Parameters

Parameter	Base Case	PCM-Enhanced
PCM	N/A	Copper
PCM thickness	N/A	0.56 mm
Solid wall thickness	0.5 mm	2 × 0.3 mm
Nominal Ref. inlet velocity	4.0 m/s	4.0 m/s
Nominal Comb. inlet velocity	4.0 m/s	4.0 m/s
Combustion flow time constant	60 s	60 s

reactor plates. Through its melting-solidification cycles, which occur at constant temperature and with only latent heat exchange, the material serves as an energy storage buffer, which absorbs excess reaction energy that may arise due to operational disturbances. The PCM layer, thus, acts as a distributed control layer that mitigates fast and potentially dangerous temperature excursions. This unconventional control system is augmented, in a hierarchical fashion, with a supervisory controller that rejects persistent disturbances.

We also introduced a novel optimization-based approach for identifying the optimal geometry of the PCM layer (i.e., for tuning the distributed controller). The proposed algorithm relies on ideas from nonlinear system identification to represent potential disturbances as PRMSs. A dynamic optimization calculation aimed at minimizing a time-integral design objective function is used. The PRMSs are imposed on the system during the time-integration steps in the optimization calculation, emulating a fast and effective Monte Carlo-type exploration of the disturbance space.

We illustrated these concepts throughout the article using a case study based on a detailed, realistic 2-D reactor model. Incorporating an input–output linearizing nonlinear feedback–feedforward supervisory controller, the proposed hierarchical control structure shows excellent disturbance rejection performance and evinces that the PCM-enhanced reactor can be operated safely under conditions that would jeopardize the structural integrity of a traditional microchannel reactor.

Although the article focuses specifically on microchannel reactors as a prototype system of elevated practical interest, the results developed in this work are completely general, and we expect that—following a thorough experimental validation—they will find applications in other process units (and, indeed, in other fields outside the chemical industry), which require controlling the temperature of small-scale, distributed-parameter systems with sensing and actuation constraints.

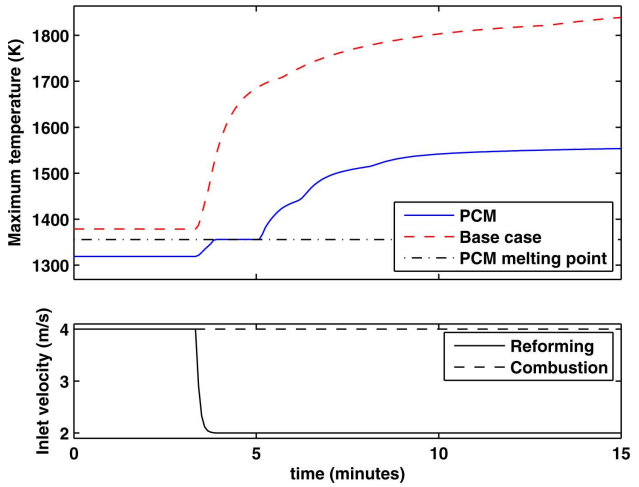

Figure 10. Maximum reactor temperature responses in base-case CPR (dashed) and PCM-enhanced CPR (solid) to 50% drop in reforming flow rate.

[Color figure can be viewed in the online issue, which is available at wileyonlinelibrary.com.]

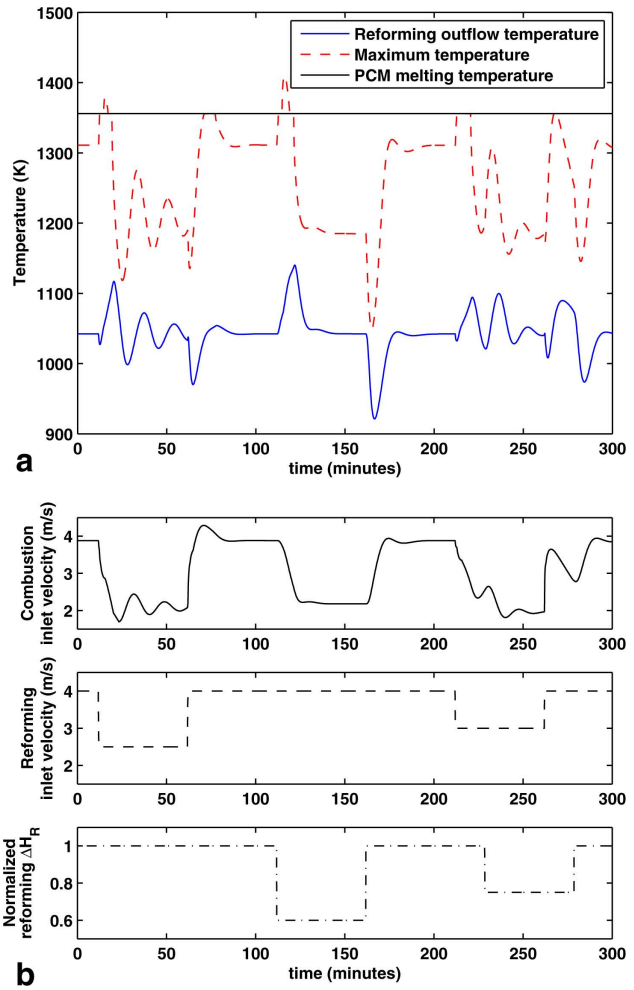

Figure 11. (a) The maximum reactor temperature (dashed) and the controlled variable, reforming outflow temperature (solid), under feedback–feedforward control during a 300-min operating period subject to disturbances in both reforming flow rate and reforming heat of reaction, (b) the combustion channel inlet velocity (manipulated variable) (solid) and reforming channel inlet velocity (dashed, disturbance 1).

The normalized reforming heat of reaction (dash-dot, disturbance 2). [Color figure can be viewed in the online issue, which is available at wileyonlinelibrary.com.]

Notation

Symbol

$a_{1\text{-}6}$ = approximate model coefficients
c = PCM cost per unit thickness, AU
c_1 = liquid PCM heat capacity, J/(kg K)
c_p = heat capacity, J/(kg K)
c_s = solid PCM heat capacity, J/(kg K)
D = diffusion coefficient, m^2/s
D_{eff} = effective diffusion coefficient, m^2/s
f = solid fraction of PCM
H = reaction heat flux, W/m^2
H^p = enthalpy of PCM, J
K = thermal conductivity, W/(m K)
L = reactor length, m
L_{ref} = reforming catalyst offset, m
L_{comp} = combustion catalyst offset, m
M = molecular weight, kg/mol
J = objective variable, AU
P = pressure, Pa
r = reaction rate, mol/(m^3 s)
r_{homog} = homogeneous reaction rate, mol/
R = radial channel thickness, m
Rg = gas constant, J/(mol K)
t = time, s
t_{final} = final simulation time, s
T = temperature, K
T_{ex}^{apprx} = approximate reforming outflow temperature, K
T_m = melting temperature of PCM, K
T_{max} = maximum temperature of PCM, K
T_r = reference temperature, K
T^{sp} = setpoint temperature, K
u = controller manipulated variable
u_z = axial velocity, m/s
u^0 = inlet velocity, m/s
W = controller disturbance variable
x = radial coordinate, m
X = local conversion
z = axial coordinate, m
δ = radial thickness, m
ΔH_{rxn} = heat of reaction, J/mol
ϵ = small parameter
η_{eff} = effectiveness factor
λ = latent heat of melting PCM, J/kg
ν = stoichiometric coefficient
ρ = density, kg/m^3
$\tau_{1,2,3}$ = control time constants, s
τ_{CL} = closed-loop time constant, s
ω = mass fraction

Superscript

cat = catalyst
g = gas phase
p = PCM
s = solid

Subscript

i = chemical species
j = channel
k = reaction

Numbering

$j = 1$ = reforming
i = CH_4,H_2O,CO,CO_2,H_2,N_2
$k = 1$ = Methane steam reforming reaction: $CH_4+H_2O \rightleftharpoons CO+3H_2$
$k = 2$ = Water–gas-shift reaction: $CO+H_2O \rightleftharpoons CO_2+H_2$
$k = 3$ = Reverse methanation reaction: $CH_4+2H_2O \rightleftharpoons CO_2+4H_2$
$j = 2$ = Combustion
i = $CH_4, O_2, CO_2, H_2O, N_2$
$k = 1$ = Methane catalytic and homogeneous combustion: $CH_4+2O_2 \rightarrow CO_2+2H_2O$

Literature Cited

1. BP Statistical Review of World Energy, 2012. Available at: http://bp.com/statisticalreview. Accessed August 1, 2012.
2. World Bank Press Release 2013/005/SDN. World bank sees warning sign in gas flaring increase. Available at: http://www.worldbank.org/en/news/2012/07/03/world-bank-sees-warning-sign-gas-flaring-increase, 2012. Accessed August 1, 2012.
3. Boerrigter, H. Economy of biomass-to-liquids (BTL) plants. Energy Research Centre of the Netherlands (ECN), 2006. Available at: www.ecn.nl/publications. Accessed August 1, 2012.
4. Van Bibber L, Shuster E, Haslbeck J, Rutkowski M, Olsen S, Kramer S. Baseline technical and economic assessment of a commercial scale (Fischer–Tropsch) liquids facility. US Department of Energy Report DOE/NETL-2007/1260, 2007.
5. Van Bibber L, Shuster E, Haslbeck J, Rutkowski M, Olsen S, Kramer S. Technical and economic assessment of small-scale (Fischer–Tropsch) liquids facilities. US Department of Energy Report DOE/NETL-2007/1253, 2007.
6. Ogugbue C, Chukwu G, Khataniar S. Economics of GTL technology for gas utilization. In: Hydrocarbon Economics and Evaluation Symposium, Dallas, TX. 1–3 April 2007.
7. Reay DA, Ramshaw C, Harvey AP. Process Intensification: Engineering for Efficiency, Sustainability and Flexibility. Oxford, UK: Butterworth-Heinemann, 2008.
8. Dietrich TR. Microchemical Engineering in Practice. Hoboken, NJ: Wiley-VCH, 2009.
9. Kolios G, Frauhammer J, Eigenberger G. Efficient reactor concepts for coupling of endothermic and exothermic reactions. In: 2nd International Symposium on Multifunctional Reactors (ISMR-2), Nurnberg, Germany, 2001. *Chem Eng Sci*. 2002;57(9):1505–1510.
10. Zanfir M, Gavriilidis A. Catalytic combustion assisted methane steam reforming in a catalytic plate reactor. *Chem Eng Sci*. 2003;58(17):3947–3960.
11. Zanfir M, Gavriilidis A. Influence of flow arrangement in catalytic plate reactors for methane steam reforming. *Chem Eng Res Des*. 2004;82(A2):252–258.
12. Baldea M, Daoutidis P. Dynamics and control of autothermal reactors for the production of hydrogen. *Chem Eng Sci*. 2007;62:3218–3230.
13. Zanfir M, Baldea M, Daoutidis P. Optimizing the catalyst distribution for countercurrent methane steam reforming in plate reactors. *AIChE J*. 2011;57(9):2518–2528.
14. Baratti R, Tronci S, Zanfir M, Gavriilidis A. Optimal catalyst distribution in catalytic plate reactors. *Int J Chem React Eng*. 2003;1:1–10.
15. Kolios G, Glockler B, Gritsch A, Morillo A, Eigenberger G. Heat-integrated reactor concepts for hydrogen production by methane steam reforming. *Fuel Cells*. 2005;5(1):52–65.
16. Annaland MV, Nijssen RC. A novel reverse flow reactor coupling endothermic and exothermic reactions: an experimental study. *Chem Eng Sci*. 2002;57(22–23):4967–4985.
17. Ramaswamy RC, Ramachandran PA, Dudukovic MP. Recuperative coupling of exothermic and endothermic reactions. *Chem Eng Sci*. 2006;61(2):459–472.
18. Xu JG, Froment GF. Methane steam reforming, methanation and water–gas shift. *1. Intrinsic kinetics. AIChE J*. 1989;35(1):88–96.
19. Cole WJ, Powell KM, Edgar TF. Optimization and advanced control of thermal energy storage systems. *Rev Chem Eng*. 2012;28(2–3):81–99.
20. Hale DV, Hoover MJ, ONeill MJ. Phase Change Materials Handbook, 1971; NASA-cr-61363.
21. Krishnan S, Garimella SV, Kang SK. A novel hybrid heat sink using phase change materials for transient thermal management of electronics. *IEEE Trans Compon Packaging Technol*. 2005;28(2):281–289.
22. Konstantinidis C, Lang W, Novoselac A. Integration of phase change materials in lightweight buildings in order to optimize the conditions for thermal comfort and to improve the building energy performance. In: Proceedings of Clima 2010, Antalya, Turkey, 2010.
23. Alexiades V, Solomon AD. Mathematical Modeling of Melting and Freezing Processes. Washington, DC; Hemisphere Publishing Corporation, 1993.
24. cnbc.com. Copper comodities index. Available at: data.cnbc.com/quotes/HGCV1 (retrieved October 26, 2012).
25. Barker HA. Design of multilevel pseudorandom signals for specified harmonic content. In: IEE Colloquium on Multifrequency Testing

for System Identification. IET, London, UK. 1990:2/1–2/6. Accessed August 1, 2012.
26. Haber R, Unbehauen H. Structure identification of nonlinear dynamic systems—a survey on input/output approaches. *Automatica*. 1990;26(4):651–677.
27. Daoutidis P, Kravaris C. Synthesis of feedforward/state feedback controllers for nonlinear processes. *AIChE J*. 1989;35(10):1602–1616.
28. Daoutidis P, Kravaris C. Dynamic output feedback control of minimum-phase nonlinear processes. *Chem Eng Sci*. 1994;49(4):433–447.
29. Cagran C. Thermal conductivity and thermal diffusivity of liquid copper. PhD thesis. Technical University of Graz, 2000.
30. Process Systems Enterprise. General PROcess Modeling System (gPROMS), 1997–2012. Available at: www.psenterprise.com/gproms.

Appendix

A. Model Equations

Gas phase

Mass balances

$$\frac{\partial \rho_j^{\mathrm{g}} \omega_{i,j}^{\mathrm{g}}}{\partial t} + \rho_j^{\mathrm{g}} u_{z_j} \frac{\partial \omega_{i,j}^{\mathrm{g}}}{\partial z} = \frac{\partial}{\partial x_j^{\mathrm{g}}} \left(\rho_j^{\mathrm{g}} D_{i-\mathrm{mix}_j} \frac{\partial \omega_{i,j}^{\mathrm{g}}}{\partial x_j^{\mathrm{g}}} \right) + \frac{\partial}{\partial z} \left(\rho_j^{\mathrm{g}} D_{i-\mathrm{mix}_j} \frac{\partial \omega_{i,j}^{\mathrm{g}}}{\partial z} \right) + \sum_k (v_{i,k,j} r_{\mathrm{homog},k,j} M_{i,j})$$

Energy balances

$$\rho_j^{\mathrm{g}} c_{pj}^{\mathrm{g}} \frac{\partial T_j^{\mathrm{g}}}{\partial t} + \rho_j^{\mathrm{g}} u_{z_j} c_{pj}^{\mathrm{g}} \frac{\partial T_j^{\mathrm{g}}}{\partial z} = \frac{\partial}{\partial x_j^{\mathrm{g}}} \left(k_j^{\mathrm{g}} \frac{\partial T_j^{\mathrm{g}}}{\partial x_j^{\mathrm{g}}} \right) + \frac{\partial}{\partial z} \left(k_j^{\mathrm{g}} \frac{\partial T_j^{\mathrm{g}}}{\partial z} \right) + \sum_k (r_{\mathrm{homog},k,j} \Delta H_{\mathrm{rxn}_{k,j}})$$

Continuity equation

$$\frac{\partial \rho_j^{\mathrm{g}}}{\partial t} + \frac{\partial \rho_j^{\mathrm{g}} u_{z_j}}{\partial z} = 0$$

Equation of state for ideal gas

$$\rho_j^{\mathrm{g}} = \frac{P_j}{R_{\mathrm{g}} T_j^{\mathrm{g}}} * \left(\sum_i \frac{\omega_{i,j}^{\mathrm{g}}}{M_{i,j}} \right)^{-1}$$

Boundary conditions

Inlet conditions

Inlet composition: $\omega_{i,j}^{\mathrm{g}} = \omega_{i,j}^{0}$

Inlet temperature: $T_j^{\mathrm{g}} = T_j^{0}$

Parabolic inlet velocity profile: $u_{z_j} = 1.5 * u_j^0 \left[1 - \left(\frac{x_j^{\mathrm{g}}}{R_j} \right)^2 \right]$

Outlet conditions

Zero flux (reforming): $\frac{\partial \omega_{i,1}^{\mathrm{g}}}{\partial z}\Big|_{z=L;\forall x_1^{\mathrm{g}}} = \frac{\partial T_1^{\mathrm{g}}}{\partial z}\Big|_{z=L;\forall x_1^{\mathrm{g}}} = \frac{\partial u_{z_1}}{\partial z}\Big|_{z=L;\forall x_1^{\mathrm{g}}} = 0$

Zero flux (combustion): $\frac{\partial \omega_{i,2}^{\mathrm{g}}}{\partial z}\Big|_{z=0;\forall x_2^{\mathrm{g}}} = \frac{\partial T_2^{\mathrm{g}}}{\partial z}\Big|_{z=0;\forall x_2^{\mathrm{g}}} = \frac{\partial u_{z_2}}{\partial z}\Big|_{z=0;\forall x_2^{\mathrm{g}}} = 0$

Channel center

Symmetry: $\frac{\partial \omega_{i,j}^{\mathrm{g}}}{\partial x_j^{\mathrm{g}}}\Big|_{x_j^{\mathrm{g}}=0;\forall z} = \frac{\partial T_j^{\mathrm{g}}}{\partial x_j^{\mathrm{g}}}\Big|_{x_j^{\mathrm{g}}=0;\forall z} = \frac{\partial u_{z_j}}{\partial x_j^{\mathrm{g}}}\Big|_{x_j^{\mathrm{g}}=0;\forall z} = 0$

Catalyst surface conditions

Material transfer: $\rho_j^{\mathrm{g}} D_{G,i-\mathrm{mix}_j} \frac{\partial \omega_{i,j}^{\mathrm{g}}}{\partial x_j^{\mathrm{g}}}\Big|_{x_j^{\mathrm{g}}=R_j;\forall z} = -\rho_j^{\mathrm{g}} D_{\mathrm{eff}i,j} \frac{\partial \omega_{i,j}^{\mathrm{cat}}}{\partial x_j^{\mathrm{cat}}}\Big|_{x_j^{\mathrm{cat}}=\delta_j^{\mathrm{cat}};\forall z}$

Energy transfer: $k_j^{\mathrm{g}} \frac{\partial T_j^{\mathrm{g}}}{\partial x_j^{\mathrm{g}}}\Big|_{x_j^{\mathrm{g}}=R_j;\forall z} = H_j + k_j^{\mathrm{s}} \frac{\partial T_j^{\mathrm{s}}}{\partial x_j^{\mathrm{s}}}\Big|_{x_j^{\mathrm{s}}=0;\forall z}$

No slip: $u_{z_j}|_{x_j^{\mathrm{g}}=R_j;\forall z} = 0$

Catalyst layer

Energy balance (isothermal in transverse direction)

$T_j^{\mathrm{cat}} = T_j^{\mathrm{g}}|_{x_j^{\mathrm{g}}=R_j}$

Mass balance

$$\frac{\partial}{\partial x_j^{\mathrm{cat}}} \left(\rho_j^{\mathrm{g}} D_{\mathrm{eff},i,j} \frac{\partial \omega_{i,j}^{\mathrm{cat}}}{\partial x_j^{\mathrm{cat}}} \right) = -\sum_k (v_{i,k,j} r_{k,j} M_{i,j})$$

Boundary conditions

Inlet conditions

Zero flux: $\frac{\partial \omega_{i,j}^{\mathrm{cat}}}{\partial z}\Big|_{z=0;\forall x_j^{\mathrm{cat}}} = 0$

Outlet conditions

Zero flux: $\frac{\partial \omega_{i,j}^{\mathrm{cat}}}{\partial z}\Big|_{z=L;\forall x_j^{\mathrm{cat}}} = 0$

Plate conditions

Zero flux: $\frac{\partial \omega_{i,j}^{\mathrm{cat}}}{\partial x_j^{\mathrm{cat}}}\Big|_{x_j^{\mathrm{cat}}=0;\forall z} = 0$

Catalyst surface conditions

Material transfer: $\omega_{i,j}^{\mathrm{g}}|_{x_j^{\mathrm{g}}=R_j;\forall z} = \omega_{i,j}^{\mathrm{cat}}|_{x_j^{\mathrm{cat}}=\delta_j^{\mathrm{cat}};\forall z}$

Effectiveness factor

$$\eta_{\mathrm{eff},k,j} = \frac{\frac{1}{\delta_j^{\mathrm{cat}}} \int_0^{\delta_j^{\mathrm{cat}}} r_{k,j} dx_j^{\mathrm{cat}}}{r_{k,j}|_{x_j^{\mathrm{cat}}=\delta^{\mathrm{cat}}}}$$

Reaction heat flux

$$H_j = \sum_k \left(-\Delta H_{k,j} \int_0^{\delta_j^{\mathrm{cat}}} r_{k,j} dx_j^{\mathrm{cat}} \right)$$

Plate

Laplace equation

$$\frac{\rho^{\mathrm{s}} c_{\mathrm{p}}^{\mathrm{s}}}{k^{\mathrm{s}}} \frac{\partial T_j^{\mathrm{s}}}{\partial t} = \frac{\partial^2 T_j^{\mathrm{s}}}{\partial z^2} + \frac{\partial^2 T_j^{\mathrm{s}}}{\partial x_j^{s^2}}$$

Boundary conditions

Inlet condition

No flux: $\frac{\partial T_j^{\mathrm{s}}}{\partial z}\Big|_{z=0;\forall x_j^{\mathrm{s}}} = 0$

Outlet condition

No flux: $\frac{\partial T_j^{\mathrm{s}}}{\partial z}\Big|_{z=L;\forall x_j^{\mathrm{s}}} = 0$

Catalyst surface

Temperature continuity: $T_j^{\mathrm{s}}|_{x_j^{\mathrm{s}}=0;\forall z} = T_j^{\mathrm{g}}|_{x_j^{\mathrm{g}}=R_j;\forall z}$

PCM layer

Energy balance

$$\rho^{\mathrm{p}} \frac{\partial H^{\mathrm{p}}}{\partial t} = \frac{\partial}{\partial z} \left(k^{\mathrm{p}} \frac{\partial T^{\mathrm{p}}}{\partial z} \right) + \frac{\partial}{\partial x^{\mathrm{p}}} \left(k^{\mathrm{p}} \frac{\partial T^{\mathrm{p}}}{\partial x^{\mathrm{p}}} \right)$$

$$T^{\mathrm{p}} = \begin{cases} T_{\mathrm{r}} + \dfrac{H^{\mathrm{p}}}{\rho c_{\mathrm{s}}} & H^{\mathrm{p}} < c_{\mathrm{s}}(T_{\mathrm{m}} - T_{\mathrm{r}}) \\ T_{\mathrm{m}} & c_{\mathrm{s}}(T_{\mathrm{m}} - T_{\mathrm{r}}) \le H^{\mathrm{p}} < c_{\mathrm{s}}(T_{\mathrm{m}} - T_{\mathrm{r}}) + \lambda \\ T_{\mathrm{m}} + \dfrac{H^{\mathrm{p}} - \lambda - c_{\mathrm{s}}(T_{\mathrm{m}} - T_{\mathrm{r}})}{c_{\mathrm{l}}} & H^{\mathrm{p}} \ge c_{\mathrm{s}}(T_{\mathrm{m}} - T_{\mathrm{r}}) + \lambda \end{cases}$$

$$f = \begin{cases} 1 & T^{\mathrm{p}} < T_{\mathrm{m}} \\ \dfrac{H^{\mathrm{p}} - c_{\mathrm{s}}(T_{\mathrm{m}} - T_{\mathrm{r}})}{\lambda} & T^{\mathrm{p}} = T_{\mathrm{m}} \\ 0 & T^{\mathrm{p}} > T_{\mathrm{m}} \end{cases}$$

Boundary conditions

Inlet condition

No flux: $\frac{\partial T^{\mathrm{p}}}{\partial z}\Big|_{z=0;\forall x^{\mathrm{p}}} = 0$

Outlet condition

No flux: $\frac{\partial T^{\mathrm{p}}}{\partial z}\Big|_{z=L;\forall x^{\mathrm{p}}} = 0$

Reforming plate

Temperature continuity: $T^{\mathrm{p}}|_{x^{\mathrm{p}}=0} = T_1^{\mathrm{s}}|_{x_1^{\mathrm{s}}=\delta_1^{\mathrm{s}}}$

Heat transfer: $k^{\mathrm{p}} \frac{\partial T^{\mathrm{p}}}{\partial x^{\mathrm{p}}}\Big|_{x^{\mathrm{p}}=0;\forall z} = k_1^{\mathrm{s}} \frac{\partial T_1^{\mathrm{s}}}{\partial x_1^{\mathrm{s}}}\Big|_{x_1^{\mathrm{s}}=\delta_1^{\mathrm{s}};\forall z}$

Combustion plate

Temperature continuity: $T^{\mathrm{p}}|_{x^{\mathrm{p}}=\delta^{\mathrm{p}}} = T_2^{\mathrm{s}}|_{x_2^{\mathrm{s}}=\delta_2^{\mathrm{s}}}$

Heat transfer: $k^{\mathrm{p}} \frac{\partial T^{\mathrm{p}}}{\partial x^{\mathrm{p}}}\Big|_{x^{\mathrm{p}}=\delta^{\mathrm{p}};\forall z} = -k_2^{\mathrm{s}} \frac{\partial T_2^{\mathrm{s}}}{\partial x_2^{\mathrm{s}}}\Big|_{x_2^{\mathrm{s}}=\delta_2^{\mathrm{s}};\forall z}$

Appendix B. Supervisory Controller Design

The first step in the design of the supervisory feedback–feedforward controller is the derivation of a suitable low-dimensional model. We proceeded by obtaining a model relating the reforming channel outlet temperature to the inlet velocities of the reforming and combustion channels (the disturbance and, respectively, manipulated variables of the system).

A steady-state analysis indicates a nonlinear relationship between the two inputs and the output, as shown in Figure A1.

The response in Figure A1 is closely approximated by a second-order polynomial of the form

$$T_{ex}^{apprx} = a_1 u^2 + a_2 w^2 + a_3 uw + a_4 u + a_5 w + a_6 \quad \text{(B1)}$$

where u and w are the manipulated (combustion flow rate) and disturbance (reforming flow rate) variables, respectively. The coefficients are, a = [−27.0, −18.6, 42.9, 74.6, −57.0, 1015]. Subsequently, we used a first-order filter of time constant τ_1 = 180 s (chosen to be of the same magnitude as the dominant time constant of the reactor, which was identified through simulations) to transform the static model B1 into an approximate dynamic model of the reactor

$$\frac{dT_{ex}^{apprx}}{dt} = \frac{1}{\tau_1}(-T_{ex}^{apprx} + a_1 u^2 + a_2 w^2 + a_3 uw + a_4 u + a_5 w + a_6) \quad \text{(B2)}$$

We then defined the auxiliary differential variables g and h, such that

$$\frac{dg}{dt} = \frac{1}{\tau_2}(-g + u) \quad \text{(B3)}$$

$$\frac{dh}{dt} = \frac{1}{\tau_3}(-h + w) \quad \text{(B4)}$$

with $\tau_2 = \tau_3 = 10$ s chosen to be much smaller than the dominant time constant of the system. With these changes, the differential model B2 can be reformulated as an input-affine system of the form

$$\dot{x} = f(x) + g(x)u + h(x)w(t) \quad \text{(B5)}$$

with

$$x = \begin{bmatrix} g \\ h \\ T_{ex}^{apprx} \end{bmatrix} f(x) = \begin{bmatrix} -g/\tau_2 \\ -h/\tau_3 \\ (a_6 - T_{ex}^{apprx})/\tau_1 \end{bmatrix}$$

$$g(x) = \begin{bmatrix} 1/\tau_2 \\ 0 \\ (a_1 g + a_3 h + a_4)/\tau_1 \end{bmatrix} h(x) = \begin{bmatrix} 0 \\ 1/\tau_3 \\ (a_2 h + a_5)/\tau_1 \end{bmatrix} \quad \text{(B6)}$$

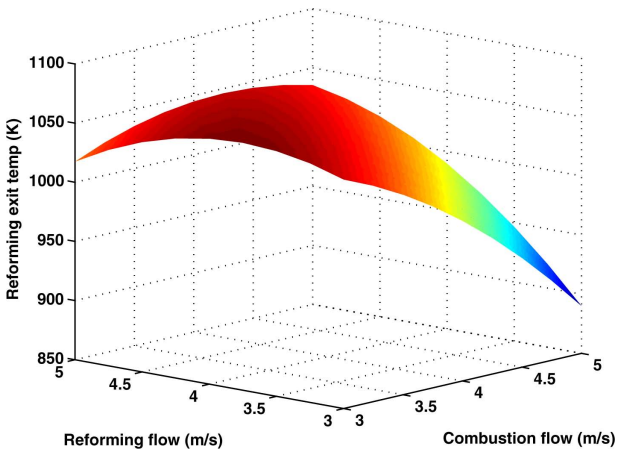

Figure A1. Surface plot of the steady-state exit reforming temperature at different combustion and reforming flow rates.

[Color figure can be viewed in the online issue, which is available at wileyonlinelibrary.com.]

which was used to derive the static control law

$$u = \frac{\tau_1/\tau_{CL}(T^{sp} - T^{ref}|_{z=L}) - a_2 wh - a_5 w - a_6 + T_{ex}^{apprx}}{a_1 g + a_3 h + a_4} \quad \text{(B7)}$$

that imposes the linear input–output closed-loop response given in Eq. 7. Note that this control law is effectively a nonlinear proportional controller, but integral action can be incorporated without difficulty.[30]

Manuscript received Sept. 20, 2012; and revision received Oct. 31, 2012.